A Fourier decomposition model predicting sound transmission and reflection of locally reacting acoustic periodic materials

Z. Zhang [1,2], **H. Denayer** [1,2], **C. Claeys** [1,2], **E. Deckers** [2,3]
[1] KU Leuven, Department of Mechanical Engineering,
Celestijnenlaan 300, B-3001, Heverlee, Belgium
e-mail: **ze.zhang@kuleuven.be**

[2] DMMS Core lab, Flanders Make, Belgium

[3] KU Leuven, Campus Diepenbeek, Department of Mechanical Engineering,
Wetenschapspark 27, B-3590, Diepenbeek, Belgium

Abstract
In this paper, an analytical model characterizing the reflected and transmitted fields of acoustic periodic structures is derived with an emphasis on phase gradient metamaterials. The model is based on a Fourier decomposition of pressure fields and connecting the incidence and the transmission sides with transfer admittance matrices. By applying pressure and velocity continuity conditions on the top and bottom surfaces of the material, the corresponding coefficient of each Fourier component of pressure fields can be determined with known admittance matrices. As a result, the model is capable of predicting reflection, transmission and absorption coefficients of phase gradient metamaterials under a given plane wave incidence. As a validation, several cases are studied using this model and compared with numerical and/or analytical predictions where a good match is found. Lastly, the limitation of the model is discussed.

1 Introduction

Acoustic periodic materials, metamaterials in particular, can be used to achieve high acoustic absorption. Regardless of the specific realizations [1–4], implementations are mainly based on minimal unit cell(s), i.e., the whole design being an infinite repetition of one or more unit cells. Given the potential of metamaterials in the field of achieving high absorption and the fact that most of them are periodic repetitions, it is of great significance to be able to predict the reflected and the transmitted fields of such a structure under plane wave incidence. The reason to study under plane wave incidence is that more complex incidence fields can be decomposed into several plane wave fields as long as the system is linear. Such a model enables one to obtain useful information (including reflection and transmission coefficients under a specific incidence) about the design itself.

In case the material is locally reacting, Mechel [5] proposed to use a spatial Fourier decomposition to predict the reflected pressure field of periodic materials that have a rigid backing. By decomposing the scattered pressure field and the surface admittance into Fourier components and applying continuity conditions at the surface of the material, each reflection component coefficient can be determined. Arguably the model is also applicable to structures without a rigid backing as long as the surface admittance is known, but it can only be used to predict the reflected field, not the transmitted field. More recent works [6–8] also focus on the application of Mechel's model to achieve high acoustic absorption but also they don't consider transmission problems.

In this paper, an extension of Mechel's model is derived to predict both the reflected and the transmitted fields

of periodic locally reacting materials. Instead of decomposing the surface admittance on the incidence side, each element of the admittance matrix which connects both sides of the material is decomposed into Fourier series. The transmitted field is also decomposed into spatial harmonics and continuity boundary conditions are also applied to both surfaces of the material. The resulting system of equations is solved using a similar approach as in [5], for the Fourier coefficients of both the reflected and the transmitted fields.

The remainder of the paper is outlined as follow. Section 2 documents the derivation of the model based on the Fourier decomposition of the pressure fields and the admittance matrices. Several validations cases are presented in section 3 ranging from a simple homogeneous layer with rigid separations to a so-called periodic phase gradient material where the material is not homogeneous. Next, the limitations of the current model are discussed in section 4. Lastly, the conclusions are summarized in section 5.

2 The Fourier decomposition model

The model described in this section uses the admittance matrix to connect both sides of the material. The admittance matrix relies on the assumption that the material it characterizes is locally reacting, i.e., waves only propagate in the direction normal to the interface inside the material. As a result, the pressure and particle velocity at different points along the interface are only coupled with their top/bottom counterpart points through admittance relations and not with any other points on the interfaces.

Considering a periodic one-dimensional structure with finite thickness which extends infinitely along the x-direction as shown in Figure 1, the incident pressure field P_i can be expressed in frequency domain as:

$$P_i = 1\,[\mathrm{Pa}] \cdot e^{-\mathrm{j}k_{ix}x} e^{\mathrm{j}k_{iy}y_1}. \tag{1}$$

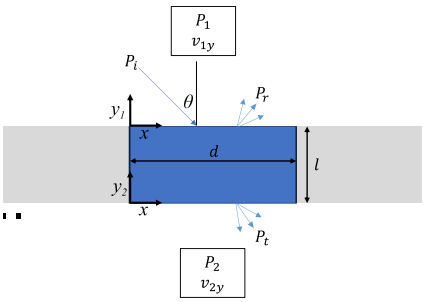

Figure 1: Schematic representation of a periodic material of infinite extent under plane wave incidence. A complete period (in the center, blue) is visualized. Each arrow in the cluster of arrows represents a certain mode in the Fourier decomposition of P_r and P_t which is equivalent to a propagating or evanescent plane wave.

Here the harmonic time dependence $e^{j\omega t}$ is assumed, but omitted for clarity. The variables k_{ix} and k_{iy} are wavenumbers in the x and y-direction, which can be defined as:

$$k_{ix} = k_0 \sin(\theta), \quad k_{iy} = k_0 \cos(\theta), \tag{2}$$

where k_0 is the free-field wavenumber in air and θ is the angle of incidence as defined in Figure 1.

The reflected and transmitted pressure fields P_r and P_t can be expressed as Fourier series due to their periodic nature:

$$P_r = \sum_{m=-\infty}^{\infty} a_{r,m} e^{-\mathrm{j}k_{x,m}x} e^{-\mathrm{j}k_{y,m}y_1}, \quad P_t = \sum_{m=-\infty}^{\infty} a_{t,m} e^{-\mathrm{j}k_{x,m}x} e^{\mathrm{j}k_{y,m}y_2}. \tag{3}$$

Each Fourier component can be regarded as either a propagating or an evanescent wave depending if its wavenumber in the y-direction has an imaginary component. Consequently, $a_{r,m}$ and $a_{t,m}$ are the m^{th}

order reflection and transmission coefficients, denoting the pressure amplitude of the m^{th} order reflected or transmitted spatial harmonic under an unitary incidence. Based on Bloch's theorem, the wavenumbers in the x and y-directions for the m^{th} order reflection and transmission are defined as [9]:

$$k_{x,m} = k_{ix} + \frac{2\pi m}{d}, \quad k_{y,m} = \mathrm{Re}\left(\sqrt{k_0^2 - (k_{x,m})^2}\right) - \mathrm{j} \cdot \mathrm{Im}\left(\sqrt{k_0^2 - (k_{x,m})^2}\right). \tag{4}$$

It should be noted that the imaginary part of $k_{y,m}$ is negative which ensures the corresponding components to be evanescent in case k_y is a complex number according to the definitions in equation (3).

The y-component of the incident, scattered and the transmitted velocity fields v_{iy}, v_{ry} and v_{ty} can be calculated from the derivative of their pressure counterparts [10]:

$$v_{iy} = -\frac{k_{iy}}{\omega\rho_0} e^{-\mathrm{j}k_{ix}x} e^{\mathrm{j}k_{iy}y_1}, \tag{5}$$

$$v_{ry} = \frac{1}{\omega\rho_0} \sum_{m=-\infty}^{\infty} a_{r,m} k_{y,m} e^{-\mathrm{j}k_{x,m}x} e^{-\mathrm{j}k_{y,m}y_1}, \tag{6}$$

$$v_{ty} = -\frac{1}{\omega\rho_0} \sum_{m=-\infty}^{\infty} a_{t,m} k_{y,m} e^{-\mathrm{j}k_{x,m}x} e^{\mathrm{j}k_{y,m}y_2}, \tag{7}$$

where ρ_0 is the air density and ω is the angular frequency.

Based on equation (1) to (7), the pressure and velocity fields on both sides of the material can be expressed as:

$$P_1(x, y_1) = P_i + P_r = 1\,[\mathrm{Pa}]\, e^{-\mathrm{j}k_{ix}x} e^{\mathrm{j}k_{iy}y_1} + \sum_{m=-\infty}^{\infty} a_{r,m} e^{-\mathrm{j}k_{x,m}x} e^{-\mathrm{j}k_{y,m}y_1}, \tag{8}$$

$$P_2(x, y_2) = P_t = \sum_{m=-\infty}^{\infty} a_{t,m} e^{-\mathrm{j}k_{x,m}x} e^{\mathrm{j}k_{y,m}y_2}, \tag{9}$$

$$v_{1y}(x, y_1) = v_{iy} + v_{ry} = -\frac{k_{iy}}{\omega\rho_0} e^{-\mathrm{j}k_{ix}x} e^{\mathrm{j}k_{iy}y_1} + \frac{1}{\omega\rho_0} \sum_{m=-\infty}^{\infty} a_{r,m} k_{y,m} e^{-\mathrm{j}k_{x,m}x} e^{-\mathrm{j}k_{y,m}y_1}, \tag{10}$$

$$v_{2y}(x, y_2) = v_{ty} = -\frac{1}{\omega\rho_0} \sum_{m=-\infty}^{\infty} a_{t,m} k_{y,m} e^{-\mathrm{j}k_{x,m}x} e^{\mathrm{j}k_{y,m}y_2}. \tag{11}$$

The admittance matrix Y connects two sides of a locally reacting material in terms of pressure and velocity, which can be expressed as:

$$v_{1y}(x, 0) = y_{11} P_1(x, 0) + y_{12} P_2(x, 0), \tag{12}$$

$$v_{2y}(x, 0) = y_{21} P_1(x, 0) + y_{22} P_2(x, 0), \tag{13}$$

where the admittance Y is expressed as:

$$Y = \begin{bmatrix} y_{11} & y_{12} \\ y_{21} & y_{22} \end{bmatrix}. \tag{14}$$

For periodic structures, each element of Y can be decomposed into a Fourier series:

$$\begin{aligned} y_{11}(x) &= \sum_{n=-\infty}^{\infty} a_n e^{-\mathrm{j}\frac{2\pi n}{d}x}, \quad y_{12}(x) = \sum_{n=-\infty}^{\infty} b_n e^{-\mathrm{j}\frac{2\pi n}{d}x}, \\ y_{21}(x) &= \sum_{n=-\infty}^{\infty} c_n e^{-\mathrm{j}\frac{2\pi n}{d}x}, \quad y_{22}(x) = \sum_{n=-\infty}^{\infty} d_n e^{-\mathrm{j}\frac{2\pi n}{d}x}, \end{aligned} \tag{15}$$

where n is an integer. The coefficients of the Fourier series can be computed from the known transfer admittance coefficients:

$$\begin{aligned} a_n &= \frac{1}{d}\int_0^d y_{11}(x)\, e^{\mathrm{j}\frac{2\pi n}{d}x}dx, \quad b_n = \frac{1}{d}\int_0^d y_{12}(x)\, e^{\mathrm{j}\frac{2\pi n}{d}x}dx, \\ c_n &= \frac{1}{d}\int_0^d y_{21}(x)\, e^{\mathrm{j}\frac{2\pi n}{d}x}dx, \quad d_n = \frac{1}{d}\int_0^d y_{22}(x)\, e^{\mathrm{j}\frac{2\pi n}{d}x}dx. \end{aligned} \tag{16}$$

Substituting equations (8) - (11) and (15) into equations (12) and (13) leads to:

$$\begin{aligned} \sum_{m=-\infty}^{\infty}\sum_{n=-\infty}^{\infty} a_n a_{r,m} e^{-\mathrm{j}\frac{2\pi(m+n)}{d}x} - \sum_{m=-\infty}^{\infty}\frac{k_{y,m}}{\omega\rho_0}a_{r,m}e^{-\mathrm{j}\frac{2\pi m}{d}x} + \sum_{m=-\infty}^{\infty}\sum_{n=-\infty}^{\infty} b_n a_{t,m} e^{-\mathrm{j}\frac{2\pi(m+n)}{d}x} \\ = -\frac{k_{iy}}{\omega\rho_0} - \sum_{n=-\infty}^{\infty} a_n e^{-\mathrm{j}\frac{2\pi n}{d}x}, \end{aligned} \tag{17}$$

$$\begin{aligned} \sum_{m=-\infty}^{\infty}\sum_{n=-\infty}^{\infty} c_n a_{r,m} e^{-\mathrm{j}\frac{2\pi(m+n)}{d}x} + \sum_{m=-\infty}^{\infty}\frac{k_{y,m}}{\omega\rho_0}a_{t,m}e^{-\mathrm{j}\frac{2\pi m}{d}x} + \sum_{m=-\infty}^{\infty}\sum_{n=-\infty}^{\infty} d_n a_{t,m} e^{-\mathrm{j}\frac{2\pi(m+n)}{d}x} \\ = -\sum_{n=-\infty}^{\infty} c_n e^{-\mathrm{j}\frac{2\pi n}{d}x}. \end{aligned} \tag{18}$$

Due to orthogonality, equation (17) and (18) can be converted into two equations per mode. The decoupling is achieved by premultiplying both sides of the two equations by $e^{\mathrm{j}\frac{2\pi o}{d}x}$ then the product is integrated over x between 0 and d. For the o^{th} mode, this leads to:

$$\sum_{m\in\mathbf{Z}} a_{o-m}a_{r,m} - \frac{k_{y,o}}{\omega\rho_0}a_{r,o} + \sum_{m\in\mathbf{Z}} b_{o-m}a_{t,m} = -\frac{k_{iy}}{\omega\rho_0} - a_o, \tag{19}$$

$$\sum_{m\in\mathbf{Z}} c_{o-m}a_{r,m} + \frac{k_{y,o}}{\omega\rho_0}a_{t,o} + \sum_{m\in\mathbf{Z}} d_{o-m}a_{t,m} = c_o. \tag{20}$$

To solve for the unknown coefficients a_r and a_t numerically, equations (19) and (20) are truncated: both o and m are limited to the range from $-N$ to N leading to the infinite sums of n to be truncated to $-2N$ to $2N$. This results into the following matrix form:

$$\begin{bmatrix} \begin{bmatrix} a_0 & \cdots & a_{-2N} \\ \vdots & \ddots & \vdots \\ a_{2N} & \cdots & a_0 \end{bmatrix} - \begin{bmatrix} \frac{k_{y,-N}}{\omega\rho_0} & & \\ & \ddots & \\ & & \frac{k_{y,N}}{\omega\rho_0} \end{bmatrix} & \begin{bmatrix} b_0 & \cdots & b_{-2N} \\ \vdots & \ddots & \vdots \\ b_{2N} & \cdots & b_0 \end{bmatrix} \\ \begin{bmatrix} c_0 & \cdots & c_{-2N} \\ \vdots & \ddots & \vdots \\ c_{2N} & \cdots & c_0 \end{bmatrix} & \begin{bmatrix} d_0 & \cdots & d_{-2N} \\ \vdots & \ddots & \vdots \\ d_{2N} & \cdots & d_0 \end{bmatrix} + \begin{bmatrix} \frac{k_{y,-N}}{\omega\rho_0} & & \\ & \ddots & \\ & & \frac{k_{y,N}}{\omega\rho_0} \end{bmatrix} \end{bmatrix} \begin{bmatrix} a_r[-N] \\ \vdots \\ a_r[N] \\ a_t[-N] \\ \vdots \\ a_t[N] \end{bmatrix} = \begin{bmatrix} -\frac{k_{iy}}{\omega\rho_0}\delta(-N,0) - a_{-N} \\ \vdots \\ -\frac{k_{iy}}{\omega\rho_0}\delta(N,0) - a_N \\ -c_{-N} \\ \vdots \\ -c_N \end{bmatrix}, \tag{21}$$

where $\delta(i,j)$ is the Kronecker delta.

As a result, the vector of unknowns a_r and a_t can be calculated by solving the system of linear equations shown in equation (21). The above group of equations make it possible to predict the reflected and transmitted pressure fields based on the known admittance matrix and period of the material. Once a_r and a_t are obtained,

the energy based reflection and transmission coefficients can be calculated as:

$$R = \frac{I_{ry}}{I_{iy}} = \frac{1}{k_0 \cos(\theta)} \sum_{m=-N}^{N} |a_{r,m}|^2 \operatorname{Re}(k_{y,m}), \tag{22}$$

$$T = \frac{I_{ty}}{I_{iy}} = \frac{1}{k_0 \cos(\theta)} \sum_{m=-N}^{N} |a_{t,m}|^2 \operatorname{Re}(k_{y,m}), \tag{23}$$

where I_{ry} and I_{ty} are the sound intensity in y-direction of the reflected and transmitted waves, I_{iy} is the y-component of the sound intensity of the incident wave where index b refers to the incident pressure field.

3 Model validation

The model presented in section 2 is denoted as FDM (Fourier decomposition model) since it relies on Fourier decomposition. In this section, the model is validated against simulations and/or analytical predictions with cases ranging from a simple homogeneous layer with equidistant rigid separations to a so-called phase gradient material where surface irregularities exist. In all cases, a good agreement is observed. For all cases considered, in the FDM model N is set to 100, which accounts for 201 modes in all computations.

3.1 An impedance matched periodic homogeneous layer with rigid separations

As a first simple case, an artificial homogeneous material of infinite extent is considered, where periodic rigid separations are included with a period of length d. Table 1 lists the basic parameters for this setup. The equivalent density and the speed of sound of the artificial material are chosen so that the material is impedance matched with air under normal incidence, meaning under normal incidence there should be no reflection. A slow speed of sound ($c_0/3$) is assigned to mimic the slow sound speed in porous materials. For the studied frequency of 2000 Hz, the wavelength of incident sound waves is 17 cm. It is therefore assumed that the studied material with a period width of 4 cm can therefore be treated as locally reacting.

Table 1: Parameters for the homogeneous layer validation setup

Period (d)	thickness (l)	Equivalent density (ρ_f)	Equivalent sound speed (c_f)	Frequency (f)
4 cm	2 cm	$3\rho_0$	$c_0/3$	2000 Hz

For comparison, the same setup is simulated numerically with a finite element model in COMSOL Multiphysics. On both sides of the domains above and below the 4 cm wide homogeneous layer, a periodic boundary condition is added. R and T from simulation are calculated similarly as in equation (22) and (23), i.e., the ratio of the y-component of the reflected and transmitted intensity over the y-component of the incident intensity. However, it should be noted that different modes are not differentiated in the simulation, i.e., only the total y-component intensities are obtained in the simulation.

Also an analytical model to calculate the R and T of the corresponding case is derived. Assuming that the material is locally reacting and that sound waves only propagate in the y-direction through the foam layer, R and T can be calculated as [11]:

$$R = \left| \frac{x_{12}\cos(\theta)^2 - Z_0 x_{11}\cos(\theta) - Z_0^2 (x_{21} - x_{22}\cos(\theta)/Z_0)}{x_{12}\cos(\theta)^2 + Z_0 x_{11}\cos(\theta) + Z_0^2 (x_{21} + x_{22}\cos(\theta)/Z_0)} \right|^2, \tag{24}$$

$$T = \left| \frac{2Z_0 e^{-\mathrm{j}k_0 l}}{x_{12}\cos(\theta)^2 + Z_0 x_{11}\cos(\theta) + Z_0^2 (x_{21} + x_{22}\cos(\theta)/Z_0)} \right|^2, \tag{25}$$

where Z_0 is the impedance of air, t_{11}, t_{12}, t_{21} and t_{22} are four elements of the transfer matrix $\mathbf{T}$, which in this case is expressed as:

$$\mathbf{T} = \begin{bmatrix} \cos(k_f l) & \mathrm{j}\rho_f c_f \sin(k_f l) \\ \frac{\mathrm{j}\sin(k_f l)}{\rho_f c_f} & \cos(k_f l) \end{bmatrix}. \tag{26}$$

The admittance matrix in equation (14) in this case can be calculated from the $\mathbf{T}$:

$$Y = \begin{bmatrix} -t_{11}/t_{12} & 1/t_{12} \\ t_{21} - t_{11}t_{22}/t_{12} & t_{22}/t_{12} \end{bmatrix}. \tag{27}$$

Figure 2 shows the comparison, where a good agreement is observed. An exact match is observed between FDM and the analytical results and a slight mismatch is observed with the COMSOL results. The discrepancy will be discussed further in section 4. One can also see that the reflection coefficient increases with angle of incidence. As expected, at normal incidence, the reflection coefficient is close to 0 and the transmission coefficient is close to 1 due to the impedance matching condition. Near grazing incidence it is the opposite which is due to the extreme impedance mismatching condition.

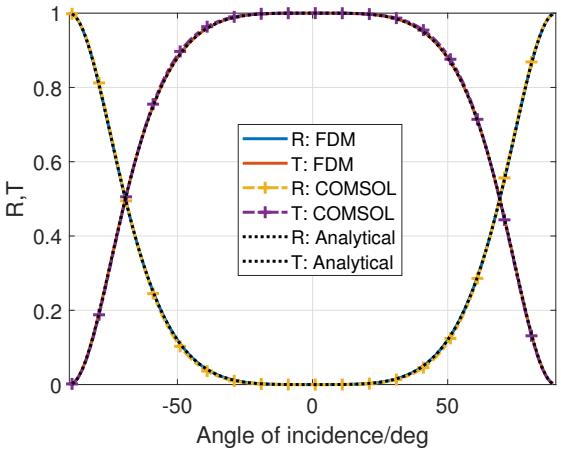

Figure 2: R and T of a homogeneous layer of infinite extent with periodic rigid separations under oblique incidence at 2000 Hz

It should be noted that for the same case with an increased thickness, the mismatching between FDM and FEM results is also increased. This will be discussed in section 4.

3.2 Two homogeneous layers forming a period

The model presented in section 2 is not limited to homogeneous materials of constant thickness, i.e., material having a constant admittance matrix along the x-axis in Figure 1. The following case extends the validation to an inhomogeneous case, where a period is composed of two homogeneous layers of the same thickness separated by hard boundaries as illustrated in Figure 3. Each element of the admittance matrix is regarded as a periodic two level staircase function along the x-axis where the values for the admittance matrix coefficients were taken from equation (27). Table 2 lists the basic parameters for this case, where clear differences exist in density and speed of sound of two materials involved. Besides, similar to the previous case, the speed of sound in both materials is lower than that in air, mimicking two different foam materials.

Table 2: Parameters for the inhomogeneous 2 homogeneous layers case

Period (d)	thickness (l)	Equivalent density (ρ_f)	Equivalent sound speed (c_f)
4 cm	2 cm	1: $3\rho_0$, 2: $4\rho_0$	1: $c_0/2$, 2: $c_0/3$

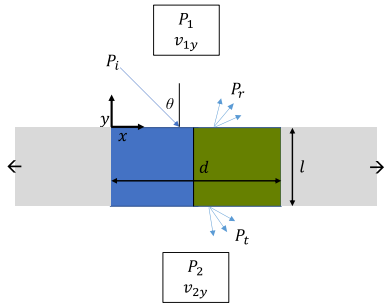

Figure 3: Schematic representation of a periodic material composed by 2 different homogeneous layers of equal width

Figure 4 shows the comparison between the finite element model and the FDM approach for this case. A good agreement is found. Here, due to impedance mismatching, even at normal incidence R is non-zero. The zero R occurs around $\pm 40°$.

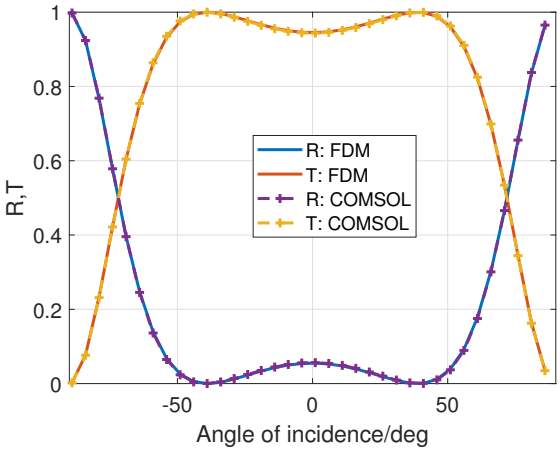

Figure 4: R and T of a periodic layer composed by two different homogeneous material layers of infinite extent under oblique incidence at 2000 Hz

3.3 An acoustic periodic structure with discretized phase gradients

As has been showed before [12], so-called phase gradient materials can yield designs of high absorption based on cells of relatively low absorption. Here, the phase gradient material under study is a periodic material composed by unit cells, as shown in Figure 5. It has been shown that a large absorption can be achieved if a perfect linear varying phase of R/T (i.e., a phase gradient with constant phase jump) exists along the metamaterial surface [13,14]. The intention of this validation is to see if the model can capture this effect and can be used to design such materials.

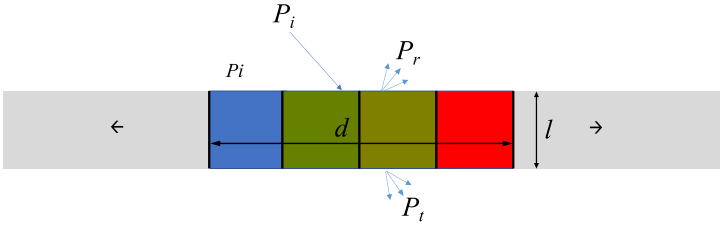

Figure 5: Schematic representation of a periodic phase gradient material. A period is discretized into 4 cells.

In Figure 5, each color block represents a homogeneous layer with a specific set of material parameters. Adjacent blocks are separated by rigid boundaries. This case can be regarded as an extension of the case described in section 3.2 where more than two homogeneous layers form a period. From here it is clear that the R and T phase will be two staircase functions with period d. Contrary to the case in section 3.2, the parameters of each homogeneous layer are selected to ensure the constant phase jump of R and T between adjacent cells of $\pi/2$ so that a discretized linear phase gradient can be formed on both the top and the bottom surfaces of the material.

For each cell in the period, the admittance matrix coefficients are obtained from the a uniform layer of this material under normal incidence which can be calculated from equation (27). As before, these coefficients are assembled into a staircase function representing the complete material. The pressure-based definition of reflection and transmission coefficients r and t of each cell under normal incidence are expressed as:

$$r = \frac{P_r}{P_i}, \qquad t = \frac{P_t}{P_i}. \tag{28}$$

Table 3 lists the setup information of this case under oblique incidence. In this case the phase of r starts from 0 for the first cell and increases by $\frac{\pi}{2}$ for each subsequent cell and a phase lag of $\frac{\pi}{2}$ between the r and t of each cell is imposed. As a result, with periodic boundary conditions on both sides a discretized linear phase gradient is formed for both r and t along x. The r and t amplitudes are taken equal with a value 0.5.

Table 3: Parameters for the oblique incidence phase gradient material

Cells per period	Period (d)	thickness (l)	r phase	t phase	$\lvert r\rvert$, $\lvert t\rvert$
4	0.5 cm	10 cm	$\left[0 : \frac{\pi}{2} : \frac{3\pi}{2}\right]$	$\left[0 : \frac{\pi}{2} : \frac{3\pi}{2}\right] + \frac{\pi}{2}$	$\lvert R\rvert = \lvert T\rvert = 0.5$

In the FEM model, each cell is characterized by an equivalent fluid model in terms of the equivalent impedance Z and the equivalent wavenumber k. From a given r and t, k and Z can be calculated by:

$$k = \pm\text{atan}\left(\frac{(r+t-1)\sqrt{-(r+t-1)(r+t+1)(r-t+1)(t-r+1)}}{(r+t+1)(-r^2+2r+t^2-1)}\right)\frac{2}{l}, \tag{29}$$

$$Z = \pm\frac{\sqrt{-(r+t-1)(r+t+1)(r-t+1)(t-r+1)}}{-r^2+2r+t^2-1}Z_0. \tag{30}$$

The comparison is shown in Figure 6, where a good match is observed except for small discrepancies on R for large angles of incidence. Furthermore, the predicted T for the complete metamaterial is always near 0 which complies to perfect phase gradient materials with an even number of cells per period, as can be inferred from the paper by Shen et. al. [6].

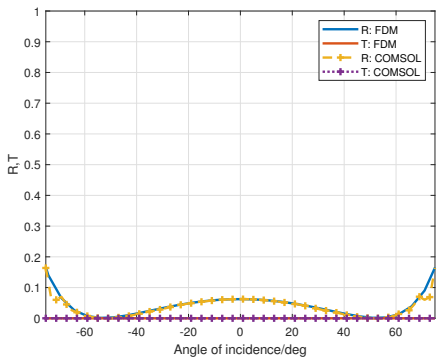

Figure 6: R and T of a phase gradient material with a period composed by 4 cells under oblique incidence, $|R| = |T| = 0.5$

4 Limitation of the model

A major limitation of the current model is that it is only accurate when d is sufficiently small compared to the wavelength. A larger d (consequently a larger cell width) can lead to oblique sound propagation within cells, which contradicts the assumption made for the admittance matrix to be valid. In other words, the FDM will turn out to be less accurate when d is large. To demonstrate this point, the case presented in section 3.1 is studied for different period widths, as listed in Table 4. The d values are chosen so that the transition of pronounced mismatching to slight mismatching can be seen. The material thickness is chosen to correspond to 1.17 times the wavelength in the material.

Table 4: Parameters for the homogeneous layer validation setup. Period width of 1, 3 and 5 cm correspond to 1/17, 1/6 and 1/3 of the wavelength at 2000 Hz.

Period (d)	thickness (l)	Equivalent density (ρ_f)	Equivalent sound speed (c_f)	Frequency (f)
1, 3, 5 cm	10 cm	$3\rho_0$	$c_0/2$	2000 Hz

Figure 7 shows the comparison between the FDM and the FEM results. It should be noted that due to the locally reacting nature of the FDM approach, the results at these different d values are the same. Thus, the R and T from only one case of the FDM approach is shown. From the figure one can see that with a decreasing d under oblique incidence the FDM approach matches better with the FEM results. This trend is indicated by the arrows, the arrow in the top left corner of the graph shows the trend for R, and the arrow at the bottom left shows the trend for T. These results confirm that a partitioned material can be considered locally reacting when the channel width d is sufficiently sub-wavelength which is the case when it is smaller than 1/15$^{\text{th}}$ of the wavelength.

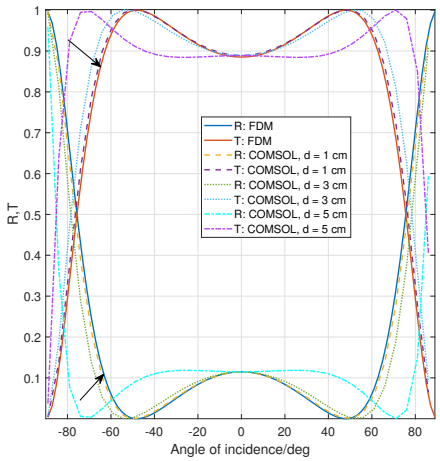

Figure 7: R and T of a partitioned homogeneous layer with infinite extent under oblique incidence at 2000 Hz

The reason for a large mismatch at a larger d is that in the FEM model the non-normal propagation within cells is considered whereas in the FDM approach only vertical propagation is assumed. With a decreasing d, in the FEM model the material behaves more and more locally reacting, meaning the assumption made in FDM becomes more and more valid. This point is further illustrated by Figure 8, where the pressure fields for several cases, as predicted by FEM are visualized. Each row in the figure represents a specific period width d and each column represents a specific angle of incidence θ. The total pressure is visualized everywhere except for the reflected region (region above the material) where only the scattered pressure is visualized for clarity. Several conclusions can be obtained from the figures. First, under oblique incidence, in-cell non-vertical propagation can be clearly seen for high values of d (last row). Second, the non-vertical propagation is more pronounced with a larger angle of incidence. Connecting these observations with the

earlier observation that a smaller d leads to a better matching between the FDM and the FEM results, one may conclude that the mismatching is indeed due to the in-cell non-vertical propagations, which cannot be accounted for accurately by the FDM due to the locally reacting assumption.

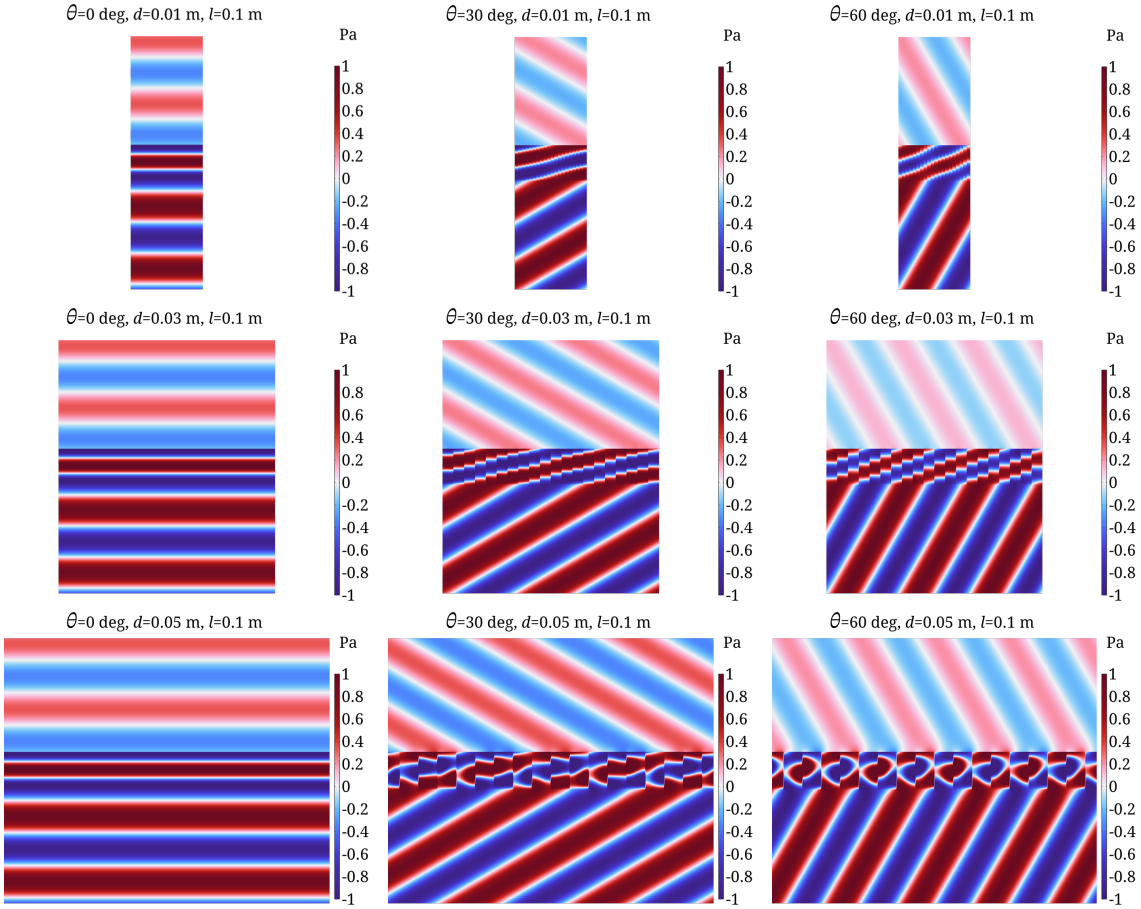

Figure 8: Pressure field of scattered field (above the material) and total pressure field (in cells and below the material) visualized at different d and θ. For each case 20 periods visualized.

A similar requirement is found on d for phase gradient materials. To study the effect of the channel width on the accuracy of the PDM for a phase gradient material, the case of section 3.3 is repeated for different period widths d under normal incidence. All other parameters are taken from table 3 and the results are compared to FEM simulations, as shown in figure 9. One can see that also here a smaller d leads to a better match with the numerical prediction, i.e., the crosses (R) in the figure go upward closer to the FDM results for R and the circles (T) shift down closer to the FDM results for T. However, the error is significantly larger than for the uniform partitioned material, where the agreement between all curves was excellent for normal incidence. This is due to the existence of high-order spatial harmonics, which are surface waves with small wavelength along the surface.

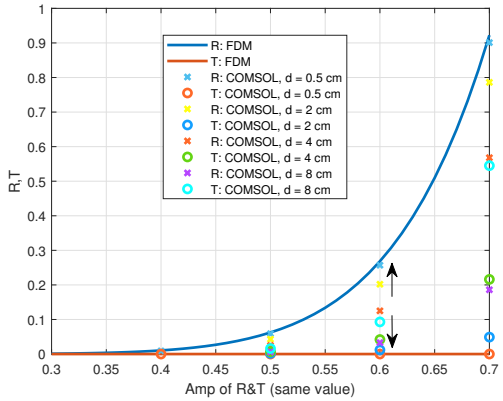

Figure 9: R and T of a phase gradient material with a period composed by 4 cells under normal incidence. d is varied and different values of R and T from the simulation observed whereas FDM gives the same result.

To further demonstrate this point, R and T of the phase gradient material of the same d and l as the previous case (parameters listed in table 5) is also predicted and compared with FEM results, as shown in Figure 10. By comparing case $d = 1\text{cm}$ of Figure 7 and 10 (both cases of the same d and l), one can see that the FDM provides a more accurate prediction for the homogeneous layer case than for the phase gradient material. This can be explained in terms of the composition of the transmitted and reflection pressure fields.

Table 5: Parameters for the oblique incidence phase gradient material

Cells per period	Period (d)	thickness (l)	r phase	t phase	$\lvert r\rvert$, $\lvert t\rvert$
4	1 cm	10 cm	$[0 : \frac{\pi}{2} : \frac{3\pi}{2}]$	$[0 : \frac{\pi}{2} : \frac{3\pi}{2}] + \frac{\pi}{2}$	$\lvert R\rvert = \lvert T\rvert = 0.5$

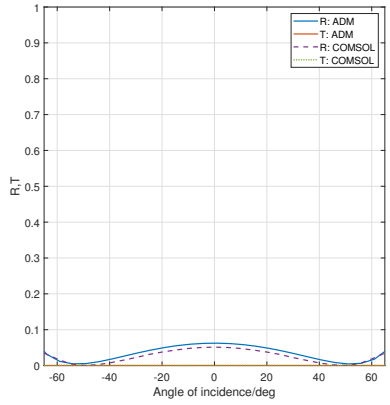

Figure 10: R and T of a phase gradient material with a period composed by 4 cells under oblique incidence, $|R| = |T| = 0.5$, $d = 1\text{cm}$

Figure 11 and Figure 12 show the modal distribution of pressure amplitude for the two cases under 50° incidence ($a_{r,m}$ and $a_{t,m}$ in equation (22) and (23)), where only modes between -5 and 5 are shown. It is clear that the phase gradient material induces the presence of multiple higher order spatial harmonics whereas the homogeneous layer only induces the 0^{th} order component. This is because for the homogeneous layer case, although the material has rigid separations embedded, the admittance matrix is still homogeneous along the surface whereas a large inhomogeneity is expected from the phase gradient case.

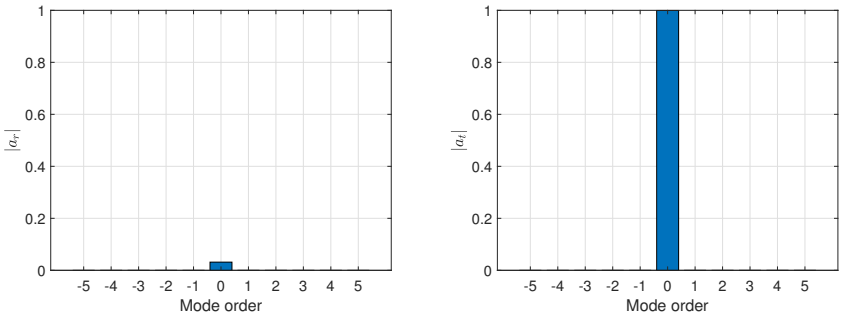

Figure 11: a_r and a_t of each mode of a homogeneous layer of infinite extent with periodic rigid separations under 50◦ incidence at 2000 Hz

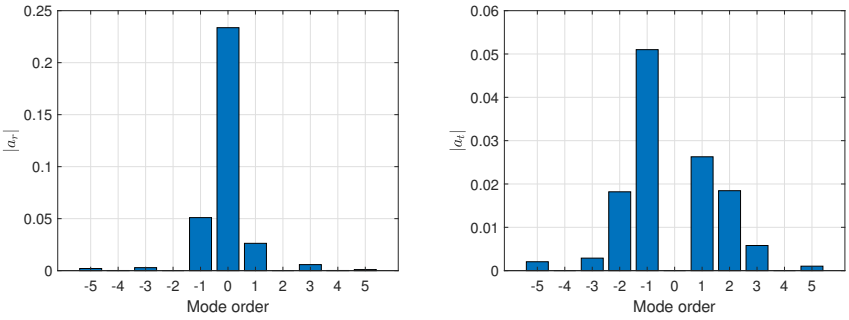

Figure 12: a_r and a_t of each mode of a phase gradient material with a period composed by 4 cells with 50° incidence, $|R| = |T| = 0.5$

When higher orders are present, although d is small compared to the wavelength in air (λ_0), the x-component of the wave number of higher order modes is large, leading to pressure and velocity fluctuations with small wavelength on the interface. For example, as is shown in Table 6, at 50° incidence, for $d = 1$ cm, d is already around 5 times of the wavelength of the $\pm 5^{\text{th}}$ order modes in the x-direction. Thus, for higher order modes this period width d can no longer be regarded as sub-wavelength, violating the locally reacting assumption made in the FDM approach. Since the working principle of a phase gradient material is to induce higher order components whereas the homogeneous layer doesn't, for the same d a worse matching is expected for the phase gradient material.

Table 6: Ratio between air wavelength and wavelength in the x-direction of each mode for $d = 1\text{cm}$ under 50° incidence

	$m=-5$	$m=-4$	$m=-3$	$m=-2$	$m=-1$	$m=0$	$m=1$	$m=2$	$m=3$	$m=4$	$m=5$
$\lvert\lambda_0/\lambda_{x,m}\rvert$	85	68	51	34	16	1	18	35	52	69	87
$\lvert d/\lambda_{x,m}\rvert$	5	4	3	2	1	0	1	2	3	4	5

In case d is large and the structure can't be considered as locally reacting, Mechel [5] proposed a model based on mode matching to account for more complex wave propagation inside each cell, where the non-axial propagation can be decomposed into different duct modes. Also in this approach, the shortcoming of Mechel's Fourier decomposition model of not being able to be applied in transmission problems can easily be alleviated.

5 Conclusions

In this paper, a model based on the Fourier decomposition is proposed to predict the reflected and transmitted fields of acoustic periodic structures. Several validation cases ranging from a simple periodic homogeneous

layer separated by rigid separations to a perfect discretized phase gradient material are used to validate this model. Results are compared with FEM simulations and/or analytical results, where in general a good match is found and also a better match is found for a material with more homogeneity. Furthermore, the limitation of the model of being mainly applicable for small period widths is shown by comparing results from several cases with varied period widths to the FEM model results. This limitation is due to assuming the material being locally reacting. It is found that the mismatch is more pronounced at large angles of incidence and larger periods. Further, it is found that if the higher order spatial harmonics are present in the reflected and transmitted fields, the sub-wavelength limitation on the period becomes more stringent as those higher order modes lead to pressure and velocity fluctuation with wavelengths that are much shorter compared to the incident wave. To overcome the limitation on period width, a mode matching method inside the cells looks promising since the non-vertical propagation in cells can then be accurately accounted for.

Acknowledgments

Internal Funds KU Leuven are gratefully acknowledged for their support.

References

[1] X. Jiang, B. Liang, R.-q. Li, X.-y. Zou, L.-l. Yin, and J.-c. Cheng, "Ultra-broadband absorption by acoustic metamaterials," *Applied Physics Letters*, vol. 105, no. 24, p. 243505, 2014.

[2] B. Cheng, H. Hou, and N. Gao, "An acoustic metasurface with simultaneous phase modulation and energy attenuation," *Modern Physics Letters B*, vol. 32, no. 23, p. 1850276, 2018.

[3] X.-F. Zhu, S.-K. Lau, Z. Lu, and W. Jeon, "Broadband low-frequency sound absorption by periodic metamaterial resonators embedded in a porous layer," *Journal of Sound and Vibration*, vol. 461, p. 114922, 2019.

[4] J. Boulvert, J. Costa-Baptista, T. Cavalieri, V. Romero-García, G. Gabard, E. R. Fotsing, A. Ross, M. Perna, J. Mardjono, and J.-P. Groby, "Folded metaporous material for sub-wavelength and broadband perfect sound absorption," *Applied Physics Letters*, vol. 117, no. 25, p. 251902, 2020.

[5] F. Mechel, "Sound fields at periodic absorbers," *Journal of sound and vibration*, vol. 136, no. 3, pp. 379–412, 1990.

[6] C. Shen and S. A. Cummer, "Harnessing multiple internal reflections to design highly absorptive acoustic metasurfaces," *Physical Review Applied*, vol. 9, no. 5, p. 054009, 2018.

[7] J. Zhou, X. Zhang, and Y. Fang, "Analytical modelling for predicting the sound field of planar acoustic metasurface," *Journal of Applied Physics*, vol. 123, no. 3, p. 033106, 2018.

[8] C. R. Liu, J. H. Wu, Z. Yang, and F. Ma, "Ultra-broadband acoustic absorption of a thin microperforated panel metamaterial with multi-order resonance," *Composite Structures*, vol. 246, p. 112366, 2020.

[9] R. E. Collin, *Field Theory of Guided Waves*, 2nd ed. IEEE-Press, 1991.

[10] F. P. Mechel, *Formulas of acoustics*. Acoustical Society of America, 2004.

[11] J. Allard and N. Atalla, *Propagation of sound in porous media: modelling sound absorbing materials 2e*. John Wiley & Sons, 2009.

[12] Z. Ze, E. Deckers, C. Claeys, H. Denayer, and W. Desmet, "Absorption enhancement by phase gradient metamaterial," in *Forum Acusticum*, 2020, pp. 2285–2290.

[13] K. Tang, C. Qiu, M. Ke, J. Lu, Y. Ye, and Z. Liu, "Anomalous refraction of airborne sound through ultrathin metasurfaces," *Sci. Rep.*, vol. 4, no. 1, pp. 1–7, 2014. [Online]. Available: https://doi.org/10.1038/srep06517

[14] Y. Xie, W. Wang, H. Chen, A. Konneker, B.-I. Popa, and S. A. Cummer, "Wavefront modulation and subwavelength diffractive acoustics with an acoustic metasurface," *Nat. Commun.*, vol. 5, no. 1, pp. 1–5, 2014. [Online]. Available: https://doi.org/10.1038/ncomms6553